PORE STRUCTURE CHARACTERIZATION OF CORE SAMPLES FROM DAQING OILFIELD BY A SYNTHESIS OF MERCURY POROSIMETRY AND IMAGE ANALISYS

[1]Baoci XU, Hongxue HAN, [2]M.A. Ioannidis, [1]Edison S. Amirtharaj, and [3]Yaru YAN
[1]Department of Earth Sciences, [2]Department of Chemical Engineering,
University of Waterloo, Waterloo, Ontario N2L 3G1, Canada
[3]Daqing Oilfield Company Ltd.
Daqing, Heilongjiang, 163500, P.R.China

This paper was prepared for presentation at the International Symposium of the Society of Core Analysts held in Toronto, Canada, 21-25 August 2005

ABSTRACT

Reservoirs in the Daqing oilfield in China are complex fluvial, lacustrine, and delta deposited heterogeneous pay zones with mixed porosities. Pore structure characterization of such media is undertaken here using a combination of mercury porosimetry and image analysis methods with the aim to determine the distribution of pore volume by pore size and estimate the pore-to-throat size aspect ratio. Central to the method used is the idea that the pore size distribution obeys a fractal scaling law over a range of pore sizes, which are accessible by both MIP and imaging methods ($.01 < r < 10$ μm). For a set of eight siltstone samples taken from a well in the Daqing oilfield, it is shown that the surface fractal dimension obtained by analysis of MIP data is consistent with the value obtained by image analysis. On this basis, scattering intensity data computed from the measured two-point correlation function in the pore size range $1 < r < 1000$ μm, are extrapolated in the size range $0.01 < r < 1$ μm using the known fractal scaling law. Then, the extended scattering intensity data are interpreted in the context of scattering by a distribution of spherical pores. This analysis provides pore size information that is consistent with Hg-air imbibition capillary pressure measurements.

INTRODUCTION

The pore structure that controls the flow and storage of fluids in sedimentary rocks is a complex network of interconnected pores, the sizes of which range from nanometers to few millimeters. The presence of local constrictions (pore throats) in the void continuum, through which pores of different size communicate, has been suggested by observation of 2D thin sections and confirmed by analysis of 3D volume data obtained by serial sectioning and X-ray computed microtomography.

A related, very important, feature of sedimentary rock microstructure is that the solid-void interface has extensive fractal properties (e.g., Katz & Thompson, 1985). Fractal scaling laws, however, cannot describe the microstructure over all length scales.

In fact, a considerable fraction of the pore volume exhibits Euclidean features and is adequately described by models derived by simulation of grain packing and compaction (e.g., Bakke & Oren, 1997) or by 3D stochastic reconstruction (e.g., Liang *et al*., 2000). The pore networks thus obtained comprise pores of angular cross-section, but do not capture quantitatively the entire spectrum of pore length scales present in real rock. As a result, attempts to predict the amount of capillary-bound water (Song *et al.*, 2000), explain the rate and extent of spontaneous imbibition (Constantinides & Payatakes, 2000), or model the electrical resistivity and relative permeability at low values of water saturation (Bekri *et al*., 2003), are not successful if pore geometry is not adequately resolved over sub-micrometric length scale, i.e., well within the size range where fractal scaling laws apply.

An experimentally validated picture of sedimentary rock, honoring length scales of the order of the grain size as well as length scales associated with microporosity, is very difficult to obtain. Numerous experimental probes of pore geometry are available (e.g., gas adsorption/condensation, small-angle scattering, mercury porosimetry, petrographic image analysis, NMR relaxometry and imaging, X-ray microtomography, etc.), yet no single imaging method can probe five or more orders of magnitude of the pore length scale, as required. Indirect methods of pore structure characterization require the introduction of fluids into the porous space, seeking to exploit the capillary properties (mercury intrusion porosimetry and N_2 gas or water vapor adsorption/condensation) or the magnetic properties (NMR relaxometry) of the solid-fluid system. Mercury intrusion porosimetry (MIP) is widely used to probe invasively the pore space in the range 20 nm to 100 μm. Unfortunately, this method *does not* provide the pore size distribution, but instead gives the distribution of pore volume accessible to mercury through pore throats of different size. Deconvolution of MIP data requires independent information on the size distribution, spatial order and interconnectedness of the pores (Tsakiroglou & Payatakes, 2000). The pore size distribution may be estimated by analyzing the NMR relaxation dynamics of fluid-saturated samples (e.g., Dunn *et al*., 2002). Such estimates hinge on the often uncertain assumptions that there is negligible averaging of magnetization by molecular diffusion between pores of different size and that the chemical properties of the solid-fluid interface are spatially uniform.

A new method of determining the pore size distribution, based on the statistical fusion of small-angle neutron scattering (SANS) and backscatter SEM (BSEM) data and their subsequent interpretation in terms of a polydispersed spherical pore (PDSP) model, has been recently proposed (Radlinski *et al*., 2004). Application of this method to a sample of reservoir sandstone has provided the pore size distribution in the range 1nm to 1mm, probing both fractal and Euclidian aspects of the microstructure. The pore size distribution thus obtained was shown to be consistent with and complementary to MIP and NMR relaxation data. The present work considers an extension of this method, whereby information generally obtained from SANS method is synthesized from MIP using surface fractal dimension based on fractal scaling law.

THEORETICAL FRAMEWORK

A porous medium may be generally described in terms of a binary phase function $Z(\mathbf{x})$, taking the value of unity if **x** points to solid and zero otherwise (Adler *et al*., 1990). The moments of the phase function $Z(\mathbf{x})$ constitute the basis for the statistical description of a microstructure with random disorder. The first two moments are readily accessible from binary BSEM images (Ioannidis et al., 1996) and correspond to the porosity and two point correlation function:

$$\phi = \langle Z(\mathbf{x}) \rangle . \tag{1}$$

$$S_2(\mathrm{r}) = \langle Z(\mathrm{x}) Z(\mathrm{x}+\mathrm{r}) \rangle , \tag{2}$$

where **r** is a lag vector and angular brackets denote statistical averages. For isotropic media the two-point correlation function $S_2(\mathrm{r})$ depends only on the modulus of the lag vector, i.e. $S_2(\mathbf{r}) = S_2(r)$. Determination of $S_2(\mathrm{r})$ from binary micrographs of the pore space is typically limited to length scales greater than about 1 μm (Ioannidis *et al*., 1996). In small-angle scattering (SAS) experiments, the measured scattering intensity *I(Q)* is the Fourier transform of the density-density correlation function $\gamma(r)$ (Glatter & Kratky, 1982):

$$I(Q) = \frac{d\sigma}{d\Omega}(Q) = 4\pi \int_0^\infty r^2 \gamma(r) \, \frac{\sin(Qr)}{Qr} \, dr \tag{3}$$

where $\gamma(r) = (\Delta\rho)^2 \phi(1-\phi) R_z(r)$ and $R_Z(r) \equiv (S_2(r) - \phi^2)/(\phi - \phi^2)$ is the void-void autocorrelation function and. In Eq (3), $(\Delta\rho)^2$ is the scattering length density contrast, a material constant depending on grain density and chemical composition, and Q is the magnitude of the scattering vector. The latter depends on the scattering angle θ and beam wavelength λ as $Q = 4\pi \sin(\theta/2)/\lambda$. For periodic structures the magnitude of the scattering vector is related to the characteristic size of the scattering object as $Q = 2\pi/r$ (Radlinski *et al*., 1999). Since rocks scatter neutrons as a quasi-two-phase system, the function $I(Q)$ measured by SANS and the function $S_2(r)$ calculated from BSEM images are a Fourier transform pair. It is on this basis that SANS and BSEM imaging information were combined to obtain the scattering cross section $I(Q)$ in the range $10^{-7} < Q < 10^{-1}$ Å^{-1} (Radlinski *et al*., 2004). Inverse Fourier transform then yielded the autocorrelation $R_z(r)$ in the size range 10 Å < *r* < 1 mm:

$$R_Z(r) = \frac{1}{2\pi^2 (\Delta\rho)^2 \phi(1-\phi)} \int_0^\infty Q^2 I(Q) \, \frac{\sin(Qr)}{Qr} \, dQ \tag{4}$$

Clearly, if $S_2(r)$ is experimentally available from BSEM images over a range of *r*-values, $I(Q)$ can be calculated in the corresponding *Q*-range using Eq. (3). The $I(Q)$ data computed in this manner are limited to relatively small *Q*-values, since the resolution of BSEM data is typically of the order of 1 μm.

It is well known that for a surface fractal object of dimension *D*, the scattering intensity follows the power law $I(Q) \propto Q^{D-6}$ with $2 < D < 3$. This scaling holds in the large Q-range, but breaks down for length scales of the order of tens of micrometers, *i.e.*, for length scales of the order of grain size. The range of pore length scales over which a fractal scaling law applies (large *Q*-range) may also be accessed by MIP. Indeed, this technique has been used to determine surface fractal dimension (*e.g.*, Ehrburger-Dolle *et al.*, 1994), yielding results in agreement with SAXS measurements (Blacher *et al.*, 2000). Fractal analysis of MIP data is based on the scaling law:

$$-dS_{Hg}/dr \propto r^{2-D} \tag{5}$$

where $S_{Hg}(r)$ is the sample saturation to mercury at capillary pressure $P_C \propto 1/r$. Eq. (5) is consistent with a scaling of the number-based pore size distribution according to the power law $f(r) \propto r^{-(D+1)}$. Over a limited range of pore length scales, $I(Q)$ data computed from $S_2(r)$ via Eq. (3) also follow the scaling $I(Q) \propto Q^{D-6}$, thus providing an estimate of *D* that can be compared to the one obtained by analysis of MIP data using Eq. (5). Provided that correspondence between the two values is established, one may extrapolate $I(Q)$ in the large *Q*-range according to $I(Q) \propto Q^{D-6}$. Thus, structural information about pore length scales not probed by BSEM may be accounted for quantitatively and consistently.

To obtain the complete distribution of pore length scales from the extended $I(Q)$ data, it is assumed that the solid-void interface has a locally spherical geometry. According to this assumption the scattering intensity per unit volume is given by (Radlinski *et al.*, 2004):

$$I(Q) = (\Delta\rho)^2 \frac{\phi}{\langle V_r \rangle} \int_{R_{\min}}^{R_{\max}} V_r^2 f(r) F_s(Qr) dr \tag{6}$$

In Eq. (6), $R_{\max}$ and $R_{\min}$ are the maximum and minimum pore radii, respectively, $V_r \equiv V(r) = (4/3)\pi r^3$ is the volume of a sphere of radius *r*, $\langle V_r \rangle = \int_{R_{\min}}^{R_{\max}} V_r f(r) dr$ is the average pore volume, $f(r)$ is the probability density of the pore size distribution, and $F_s(Qr)$ is the form factor for a sphere of radius r:

$$F_s(Qr) = \left[3 \frac{\sin(Qr) - Qr\cos(Qr)}{(Qr)^3} \right]^2 \tag{7}$$

The function $f(r)$ is determined by inversion of the extended $I(Q)$ data using Eq. (6). The cumulative distribution of pore volume by *pore size* is then computed from $f(r)$ and plotted along mercury porosimetry data as a function of equivalent capillary pressure for purposes of comparison.

RESULTS AND DISCUSSION

A total of 8 rock samples from the Daqing oil field, China, were studied in this work. Core and log measurements of porosity and permeability are listed in Table 1. Also included in Table 1 are image analysis data, such as the porosity, image resolution and integral correlation length scale Λ – the latter determined from the measured void-void autocorrelation function as follows:

$$\Lambda = \int_0^\infty R_Z(r)dr \tag{8}$$

Mercury porosimetry tests (intrusion and extrusion) were performed on 1-cc cubic samples coated with epoxy on all but one face to minimize surface penetration effects. These tests were carried out to a maximum capillary pressure of 40000 psia, stepping pressure to increasing values only after equilibration of the mercury volume. Additionally, low pressure (1-50 psi) intrusion and extrusion tests were also carried out on all the samples.

Table 1 reveals that the porosity computed by image analysis agrees with core analysis values for most of the samples. Estimates of fractal dimension, D, by MIP and image analysis are also in good agreement for the majority of the samples. Permeability predictions from porosity and Λ using an empirical equation proposed by Ioannidis *et al*. (1996) agree with log analysis values to within a factor of two.

The computation of I(Q) data from binary images and MIP data and the interpretation of these data to obtain the pore size distribution is illustrated in Figure 1 using sample #2 as an example. Figure 1(a) shows how the surface fractal dimension is calculated from MIP data using Eq (5). This analysis yields D = 2.51. The plot suggests an upper cut-off of the fractal scaling near r = 10 μm, implying that a significant amount of pore volume may be attributed to a surface fractal. It is noted, however, that deviation from linearity in this plot does not mean that $f(r) \propto r^{-(D+1)}$ is not obeyed, since $S_{Hg}(r)$ is also sensitive to pore accessibility limitations. Accessibility effects are predominant in the vicinity of the percolation threshold, as evidenced by the peak of the dS_{Hg}/dr data near $r = 25\mu m$. Figure 1(b) shows the trend $I(Q) \propto Q^{D-6}$, with D = 2.51, of the $I(Q)$ data computed via Eq (3) from the average image statistical properties. The fitting of the extended $I(Q)$ data by Eq. (6) produces the pore size distribution $f(r)$ shown in Fig. 1(c). This distribution obeys $f(r) \propto r^{-(D+1)}$ with D = 2.51 for pore length scales up to about $r = 50\mu m$ indicating that the great majority of the pore volume may be attributed to a surface fractal.

The cumulative pore volume distribution calculated from the $f(r)$ is compared to the mercury porosimetry data in Fig. (2) for each sample studied. The following observations may be made. First, the pore volume distribution (PVD) spans five orders of magnitude of the length scale. Second, the PVD has significant overlap with the low pressure extrusion curve. Since the length scale controlling the capillary pressure for mercury extrusion corresponds to the pore size, this agreement lends quantitative support to the conclusion that the distribution $f(r)$ is a pore size distribution.

Obviously, mercury extrusion data furnish no information about the size of pores from which mercury does not retract, either because the capillary pressure is not sufficiently low or because it mercury in these pores is trapped.

The combined effect of the presence of local constrictions in the pore space (pore throats) and of limited pore accessibility due to the interconnectivity and spatial arrangement of pores of different sizes, manifests itself as a shift between the distribution of *accessible* pore volume by pore throat size (measured by the mercury intrusion curve) and the PVD. An *apparent* pore-to-throat size aspect ratio may be defined as the pore-to-throat aspect ratio r_p / r_t that would bring the two distributions of pore volume into coincidence. In Fig. (2), a constant pore-to-throat aspect ratio is seen to bring the two distributions in reasonable coincidence for the majority of the samples studied. More precise values are given in Fig. (3) and Fig. (4). It is emphasized that accessibility limitations, which are more pronounced for pores of the largest sizes, cause the apparent pore-to-throat aspect ratio attributed to these pores to be greater than the actual one.

CONCLUSIONS

By combining mercury porosimetry and image analysis data within a statistical framework, the distribution of pore volume by pore size over the entire range of pore length scales was determined for a suite of siltstones samples from the Daqing oil field (China). The results have demonstrated significant similarities in the pore structure of all but one sample (sample #8), in qualitative agreement with the results of mercury intrusion/extrusion tests. A correlation between an apparent pore-to-throat size aspect ratio and residual non-wetting phase saturation during quasi-static imbibition of a strongly wetting phase is suggested by the data.

REFERENCES

1. Adler, P.M., Jacquin, C.G. & Quiblier, J.A. (1990). Flow in simulated porous media. *International Journal of Multiphase Flow, 16*, 691.

2. Bakke, S. & Oren, P. (1997). 3D pore-scale modeling of sandstones and flow simulations in pore networks. *SPE Journal, 2*(2), 136-149.

3. Bekri, S., Howard, J., Muller, J. & Adler, P.M. (2003). Electrical resistivity index in multiphase flow through porous media. *Transport in Porous Media, 51*, 41-65.

4. Blacher, S., Heinrichs, B., Sahouli, B., Pirard, R. & Pirard, J.-P. (2000). Fractal characterization of wide pore range catalysts: Application to Pd–Ag/SiO_2 xerogels. *Journal of Colloid and Interface Science, 226*, 123-130.

5. Constantinides, G.N. & Payatakes, A.C. (2000). Effects of precursor wetting films in immiscible displacement through porous media. Transport in Porous Media, 38, 291-317.

6. Dunn, K.J., Bergman, D.J. & LaTorraca, G.A. (2002). Nuclear magnetic resonance: Petrophysical and logging applications. In: K. Helbig & and S. Treitel (eds), Handbook of geophysical exploration, vol. 32, Oxford, Pergamon Press.

7. Ehrburger-Dolle, F., Lavanchy, A., & Stoeckli, F. (1994). Determination of the surface fractal dimension of active carbons by mercury porosimetry. Journal of Colloid and Interface Science, 166, 451-461.

8. Glatter, O. & Kratky, O. (1982). Small-angle X-ray scattering. London: Academic Press.
9. Ioannidis, M.A., Kwiecien, M.J. & Chatzis, I. (1996). Statistical analysis of the porous microstructure as a method for estimating reservoir permeability. Journal of Petroleum Science and Engineering, 16, 251-261.
10. Katz, A.J. & Thompson, A.H. (1985). Fractal sandstone pores: Implications for conductivity and pore formation. Physical Review Letters, 54, 1325-1328.
11. Liang, Z., Ioannidis, M.A. & Chatzis, I. (2000). Permeability and electrical conductivity of porous media from 3D stochastic replicas of the microstructure. Chemical Engineering Science, 55, 5247-5262.
12. Radlinski, A.P., Radlinska, E.Z., Agamalian, M., Wignall, G.D., Lindner, P., & Randl, O.G. (1999). Fractal geometry of rocks. Physical Review Letters, 82, 3078-3081.
13. Radlinski, A.P., Ioannidis, M.A., Hinde, A.L., Hainbuchner, M., Baron, M., Rauch, H. & Kline, S.R. (2004). Angstrom to millimeter characterization of sedimentary rock microstructure. Journal of Colloid and Interface Science.
14. Song, Y.Q., Ryu, S.G. & Sen, P.N. (2000). Determining multiple length scales in rocks. Nature, 406, 178-181.
15. Tsakiroglou, C.D. & Payatakes, A.C. (2000). Characterization of the pore structure of reservoir rocks with the aid of serial sectioning analysis, mercury porosimetry and network simulation. Advances in Water Resources, 23, 773-789.

Table 1. Summary of petrophysical and image analysis measurements.

Code	Lithology[1]	k_{core}[1] (mD)	k_{log}[1] (mD)	k_{pred} (mD)	ϕ[1]	Resolution (μm/pixel)	ϕ_{img}	Λ (μm)	D_{img}	ϕ_{MIP}	D_{MIP}
1	Siltstone	4254	1180	2217	0.306	1	0.304	29.89	2.61	0.397	2.76
2	Siltstone	840	543	1336	0.322	1	0.329	17.70	2.51	0.274	2.51
3	Siltstone	6568	1189	2389	0.308	1	0.260	30.63	2.72	0.233	2.72
4	Siltstone	2823	1194	669	0.308	1	0.280	13.98	2.68	0.255	2.82
5	Siltstone	2823	1194	1634	0.308	1.15	0.306	23.88	2.6	0.280	2.72
6	Siltstone	454	855	1498	0.280	1.43	0.297	32.31	2.61	0.255	2.61
8	Siltstone	56	152	696	0.303	0.833	0.20	14.53	2.9	0.187	3
10	Siltstone	311	999	967	0.304	0.666	0.296	17.79	2.64	0.242	2.64

[1]Data supplied by Daqing Oilfield Company, Daqing, PR China.

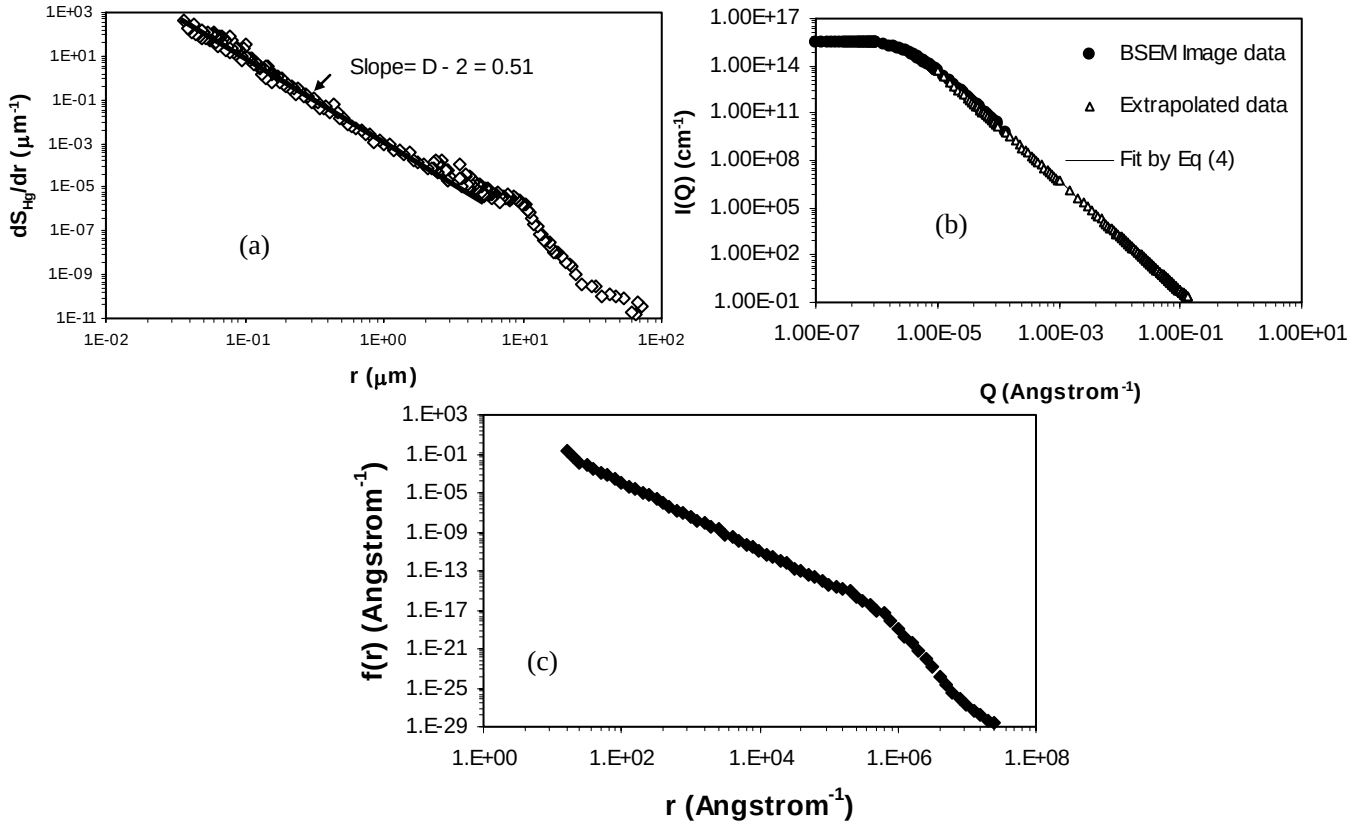

Figure 1. Statistical fusion of MIP and BSEM microstructure data (sample #2): (a) determination of surface fractal dimension from MIP data; (b) Extrapolation and fitting of $I(Q)$ data; (c) complete pore size distribution.

(a) Sample #1

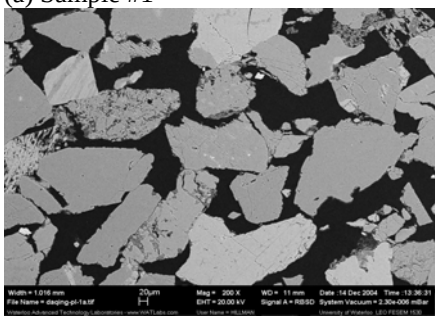

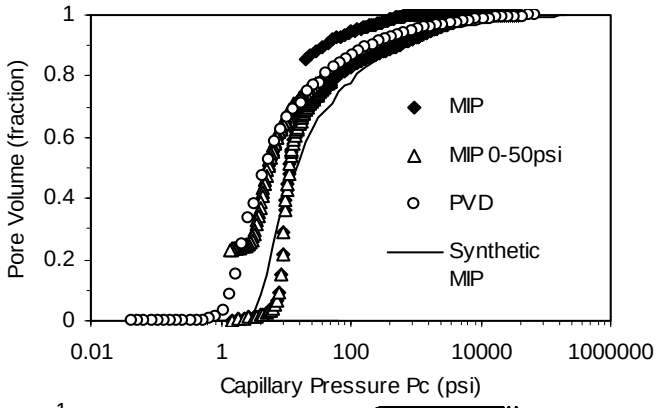

(b) Sample #2

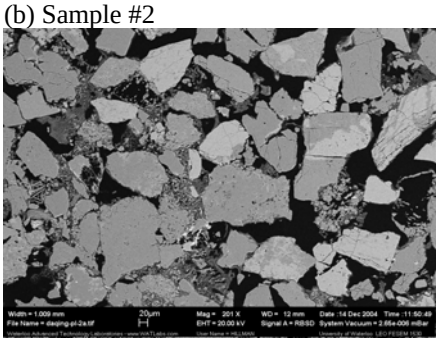

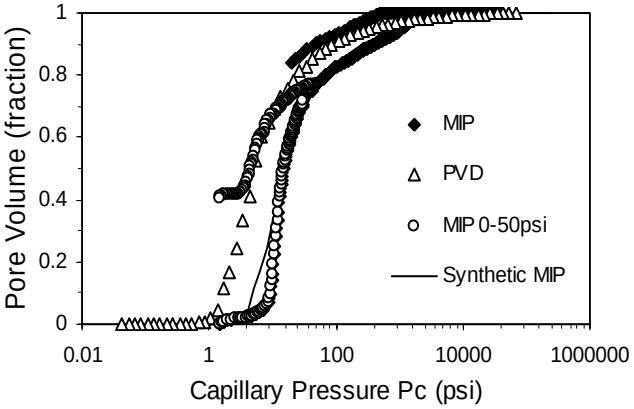

(c) Sample #3

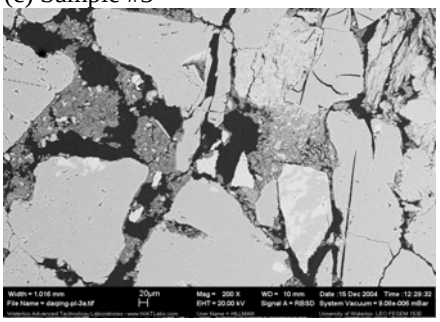

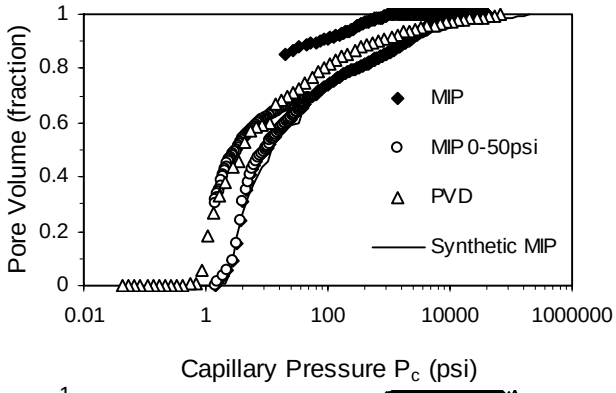

(d) Sample #4

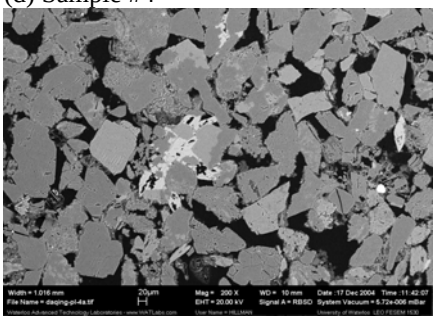

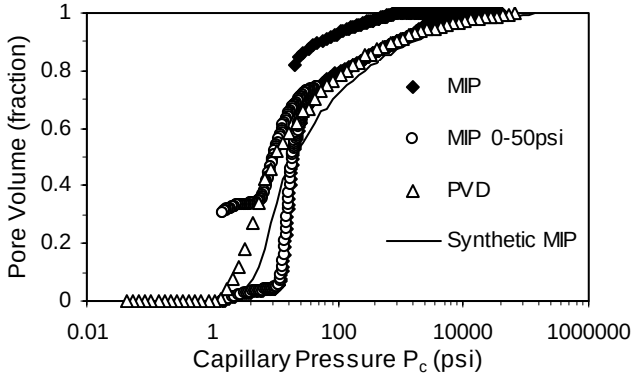

(e) Sample #5

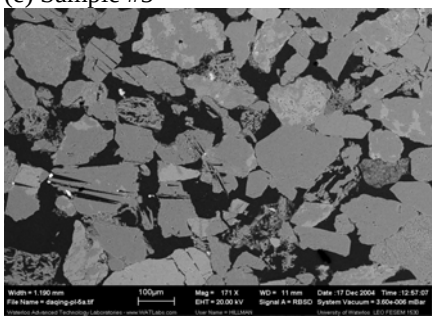

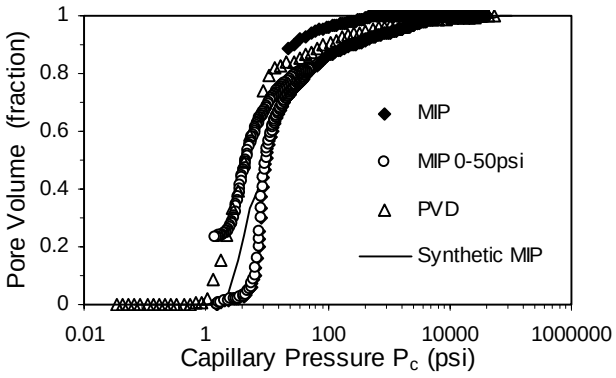

(f) Sample #6

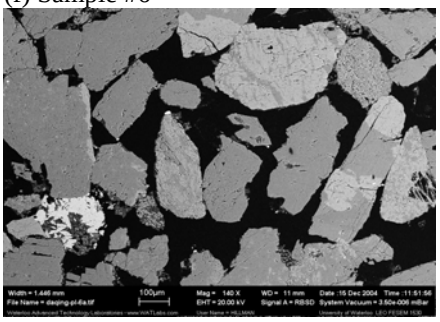

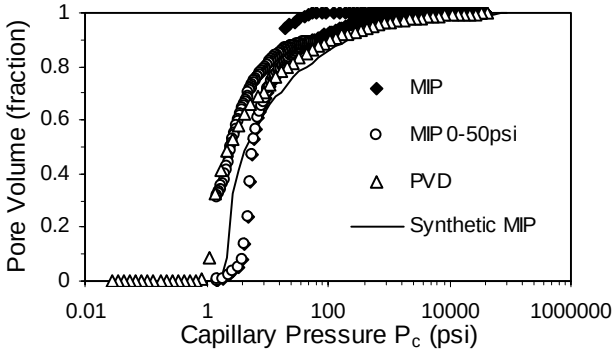

(g) Sample #8

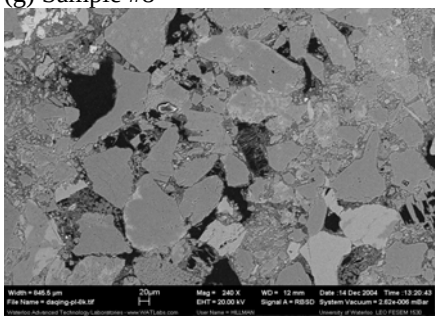

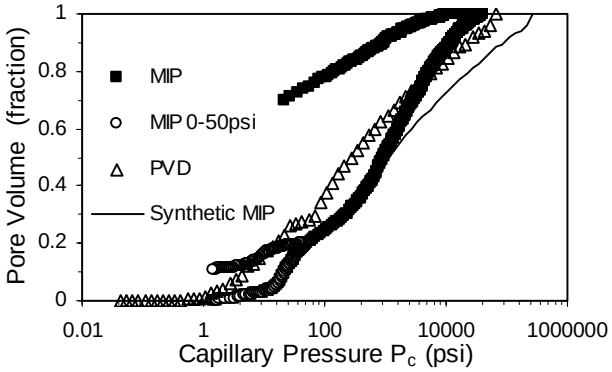

(h) Sample #10

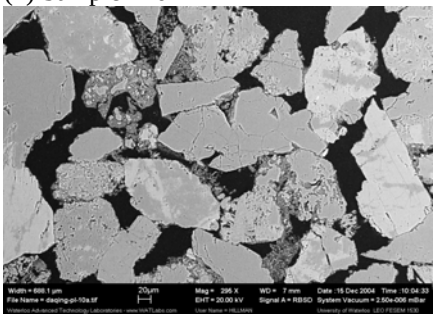

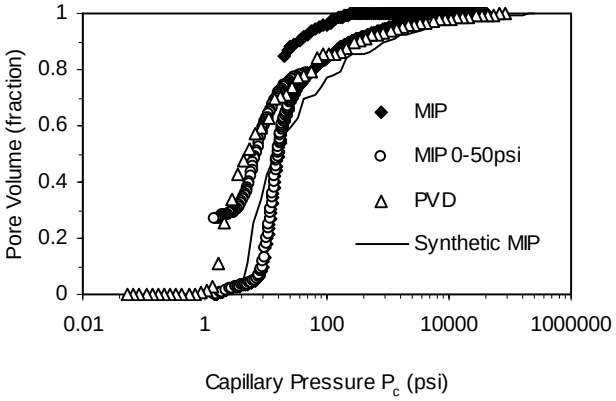

Figure 2. Distribution of pore volume by pore size (PVD), distribution of accessible pore volume by pore throat size (MIP) and simulated MIP result assuming complete pore accessibility and constant pore-to-throat aspect ratio of (a) 3, (b) 3, (c)3 (d) 2, (e) 2, (f) 2, (g) 4 and (h) 3.

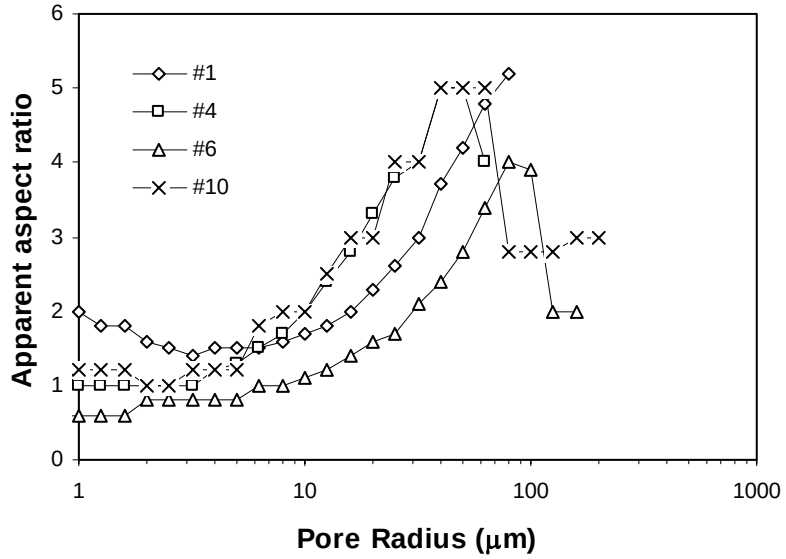

Figure 3. Apparent pore-to-throat aspect ratio for samples 1, 4, 6, 10.

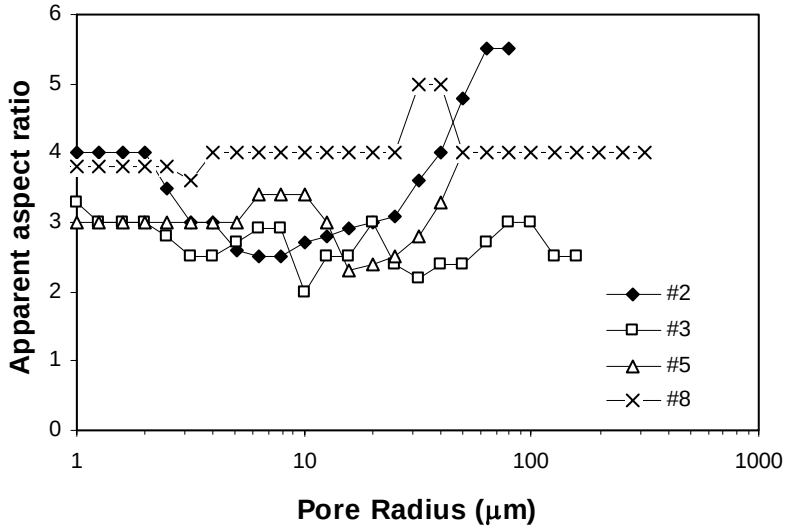

Figure 4. Apparent pore-to-throat aspect ratio for samples 2,3,5,8.